molecules

MDPI

Article

Core–Shell CoS_2@MoS_2 with Hollow Heterostructure as an Efficient Electrocatalyst for Boosting Oxygen Evolution Reaction

Donglei Guo [1], Jiaqi Xu [1], Guilong Liu [1] and Xu Yu [2,*]

[1] Key Laboratory of Function-Oriented Porous Materials, College of Chemistry and Chemical Engineering, Luoyang Normal University, Luoyang 471934, China; gdl0594@163.com (D.G.); 18836032666@163.com (J.X.); glliu@tju.edu.cn (G.L.)

[2] Institute of Innovation Materials and Energy, School of Chemistry and Chemical Engineering, Yangzhou University, Yangzhou 225002, China

* Correspondence: yxypz15@yzu.edu.cn

Abstract: It is imperative to develop an efficient catalyst to reduce the energy barrier of electrochemical water decomposition. In this study, a well-designed electrocatalyst featuring a core–shell structure was synthesized with cobalt sulfides as the core and molybdenum disulfide nanosheets as the shell. The core–shell structure can prevent the agglomeration of MoS_2, expose more active sites, and facilitate electrolyte ion diffusion. A CoS_2/MoS_2 heterostructure is formed between CoS_2 and MoS_2 through the chemical interaction, and the surface chemistry is adjusted. Due to the morphological merits and the formation of the CoS_2/MoS_2 heterostructure, CoS_2@MoS_2 exhibits excellent electrocatalytic performance during the oxygen evolution reaction (OER) process in an alkaline electrolyte. To reach the current density of 10 mA cm^{-2}, only 254 mV of overpotential is required for CoS_2@MoS_2, which is smaller than that of pristine CoS_2 and MoS_2. Meanwhile, the small Tafel slope (86.9 mV dec^{-1}) and low charge transfer resistance (47 Ω) imply the fast dynamic mechanism of CoS_2@MoS_2. As further confirmed by cyclic voltammetry curves for 1000 cycles and the CA test for 10 h, CoS_2@MoS_2 shows exceptional catalytic stability. This work gives a guideline for constructing the core–shell heterostructure as an efficient catalyst for oxygen evolution reaction.

Keywords: molybdenum disulfide; core–shell structure; heterostructure; oxygen evolution; Prussian blue

Citation: Guo, D.; Xu, J.; Liu, G.; Yu, X. Core–Shell CoS_2@MoS_2 with Hollow Heterostructure as an Efficient Electrocatalyst for Boosting Oxygen Evolution Reaction. *Molecules* **2024**, *29*, 1695. https://doi.org/10.3390/molecules29081695

Academic Editors: Panpan Zhang and Wenjing Yuan

Received: 21 March 2024
Revised: 4 April 2024
Accepted: 6 April 2024
Published: 9 April 2024

1. Introduction

Exploring clean and renewable energy to substitute traditional fossil fuels is important to alleviate the current global environmental problems [1,2]. Hydrogen energy with high gravimetric energy density and pollution-free characteristics has been considered as a potential energy source in many applications [3,4]. Oxygen evolution reaction (OER), as a half-reaction of electrocatalytic water splitting, is a complicated four-electron transfer process, and the sluggish kinetics still need to be improved to enhance the efficiency of water electrolysis [5]. Conventional water electrolysis often relies on noble metals, such as platinum and ruthenium-based catalysts [6–9], which exhibit fast kinetic behavior and low overpotential. Despite these merits of noble-metal catalysts, the high prices and rarity of resources severely inhibit their widespread application [10], and the development of cheap and effective catalysts has attracted attention to improve the dynamic reaction [11].

Recently, transition-metal-based composites with earth-abundant sources and high efficiency have been proposed to substitute noble-metal catalysts. Many kinds of metal composites, including metal sulfides [12–15], metal phosphides [16,17], and metal oxides/hydroxides [18–20], have been demonstrated to show improved catalytic OER activity in an alkaline electrolyte. As confirmed by computational and experimental analyses, cobalt sulfides with a refined surface chemical state can be used as effective catalysts to facilitate the electrochemical reaction during the OER process [21,22]. Apart from modifying the

composition, a delicate structural design is also important for improving the electrocatalytic performance. Great attention has been paid to develop Prussian blue analog (PBA)-based nanomaterials in the application of energy storage and conversion systems [23,24], while the poor electrical conductivity and inertness of intrinsic activity prevent the application of pristine PBA nanomaterials for OER [25]. The regulation of the adsorption energy of active sites and the improvement of intrinsic conductivity can be modified by the incorporation of heteroatoms (S, P, Se, F, etc.) [26–29]. Metal sulfides derived from the Prussian blue analog can hold structural and compositional merits, and a hollow structure can be derived by ion exchange during the hydrothermal reaction process, which is favorable for accelerating electrolyte ion diffusion and facilitating charge transfer [25,27,30]. PBA derivatives with porous structures can expose the large specific surface area and increase the utilization of active sites. Furthermore, introducing the second functional into the PBA derivatives is a promising strategy to improve the catalytic OER activity of catalysts.

Transition-metal dichalcogenides (TMDCs) with layered structures have been proposed as economical and efficient catalysts, and have been proven to have highly efficient activity in the dominant electrochemical reaction process of oxygen evolution reaction [31,32]. Most possible reasons for this include the exposure of active basal and edge sites to accelerate the reaction kinetics and the modification of the intrinsic activity of layered nanosheets. Many efforts have been made to reduce the charge transfer resistance of TMDCs by the incorporation of heteroatoms and the formation of heterostructures [21,33,34]. Molybdenum disulfide (MoS_2), with a metallic 1T crystal structure, shows improved catalytic OER performance by activating intrinsic activity on the basal plane and edge sites [35–37]. The surface's defective sites can be modified to change the electronic structure and boost the active sites. However, the restacking and aggregation of layered MoS_2 are still key issues to be solved. The core–shell morphology of the catalyst can show specific physical properties and surface chemistry, which is beneficial to expose the large surface area and active sites, effectively protect the active surface, inhibit the aggregation of layered material, and optimize the electronic structure, resulting in the improvement of catalytic behaviors [38]. Therefore, the construction of a heterostructure can further improve the catalytic OER performance by forming strong interfaces between two different transition metal components [39–41], while the controllable morphology of the heterostructure can efficiently prevent the aggregation of layered TMDCs [42,43]. Despite the above issues, we aimed to construct a layered TMDC-based catalyst to develop the OER performance of a compositional-adjusted CoS_2@MoS_2 heterostructure.

In this work, we prepared a hollow CoS_2@MoS_2 heterostructure with a core–shell structure through hydrothermal and sulfidation processes. The vertically aligned structure, revealed by microscopic analysis, guarantees the distribution of MoS_2 nanosheets without aggregation and provides abundant channels for electrolyte diffusion. The surface chemistry of CoS_2@MoS_2 is tuned by the existence of 1T-phase MoS_2 and a strong electrochemical interaction at the CoS_2/MoS_2 interface. On account of the heterostructure and modified chemical state, CoS_2@MoS_2 shows excellent catalytic OER performance, such as low overpotential, a small Tafel slope, low charge transfer resistance, and good electrochemical stability.

2. Results and Discussion

2.1. Synthesis and Characterization of CoS_2@MoS_2

As illustrated in Figure 1a, the cobalt-sulfide-coupled molybdenum disulfide (CoS_2@MoS_2) nanocube with a core–shell structure was prepared using co-precipitation, low-temperature sulfurization, and hydrothermal methods. In brief, the cobalt Prussian blue analog (Co-PBA) was initially synthesized using the precipitation method at room temperature and further treated by low-temperature sulfurization to obtain the CoS_2 nanocube. After mixing with the Mo precursor, the interlaced MoS_2 nanosheets were grown on the surface of the CoS_2 nanocube during the hydrothermal process, and the core–shell CoS_2@MoS_2 catalyst was finally obtained. Scanning electron microscopy (SEM) was carried out to characterize

the morphology of the CoS_2@MoS_2. As shown in Figure 1b, the surface of the Co-PBA nanocube is smooth and the average size of the diameter is about 200 nm. After the initial sulfurization, the CoS_2 showed a hollow structure arising from the ion exchange of Co, and the roughness of the surface increased due to the formation of metal sulfide nanoparticles (Figure 1c). Furthermore, MoS_2 nanosheets were vertically aligned on the CoS_2 nanocube, which efficiently inhibited the aggregation of MoS_2 nanosheets, as shown in Figure 1d. It can be found that the average diameter of CoS_2@MoS_2 is larger in contrast to the hollow CoS_2 nanocube due to the growth of MoS_2 on the surface. The increased roughness and porous surface are favorable as they provide a large surface area and sufficient channels for electrolyte ion diffusion.

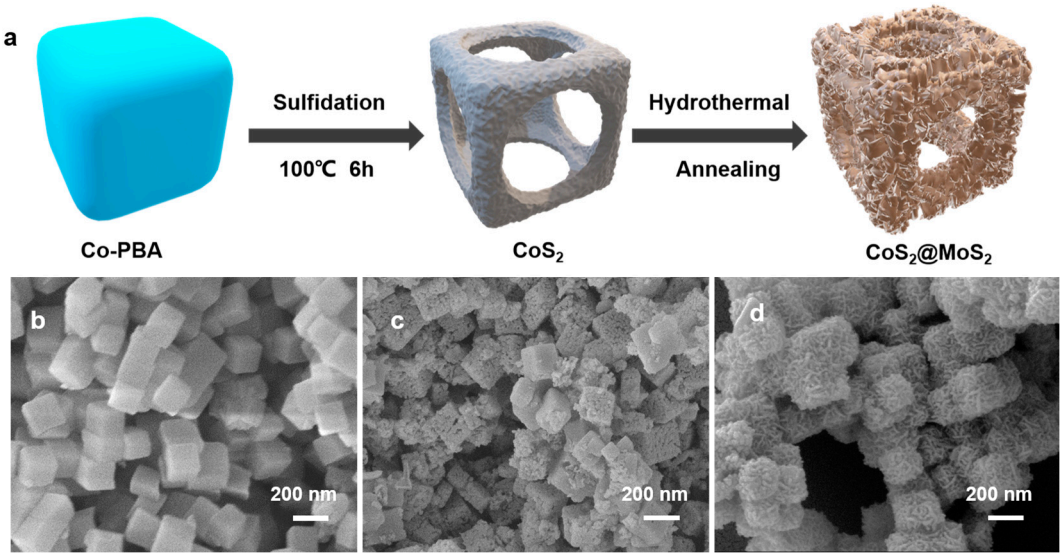

Figure 1. (**a**) Schematic illustration of the synthesis process of CoS_2@MoS_2. SEM images of (**b**) Co-PBA, (**c**) CoS_2, and (**d**) CoS_2@MoS_2.

The morphology of CoS_2@MoS_2 was further investigated using transmission electron microscopy (TEM), as shown in Figure 2. Figure 2a shows the TEM image of pristine Co-PBA with a transparent morphology and smooth surface, which is consistent with the SEM result. After sulfurization treatment, the hollow structure of the CoS_2 nanocube can be observed, and the rough surface is composed of metal sulfides (Figure 2b). As shown in Figure 2c, the MoS_2 nanosheets are uniformly grown and distributed on the CoS_2 surface to form the core–shell structure. From the high-magnification TEM image in Figure 2d, two different lattice fringes can be observed, which are intertwined with each other, and the values of interplanar spacing of 0.63 and 0.20 nm correspond to the (002) plane of MoS_2 and the (220) plane of CoS_2. In particular, the interplanar spacing of MoS_2 for CoS_2@MoS_2 is larger than that of pristine MoS_2, and the expanded d-spacing results from the hybridization of CoS_2 with MoS_2 nanosheets.

X-ray diffraction was applied to evaluate the crystal structure of the CoS_2@MoS_2, as shown in Figure 3a. The apparent characterization peak at ~14.1° corresponds to the (002) plane of MoS_2 [33], and another three peaks are indexed to the presence of CoS_2 [PDF#41-1471], implying that CoS_2@MoS_2 consists of MoS_2 and CoS_2. X-ray photoelectron spectroscopy (XPS) was used to evaluate the surface chemical state and electronic structure of CoS_2@MoS_2, and the C 1s peak at 284.6 eV was used to calibrate all of the spectra. CoS_2@MoS_2 consists of Mo, C, O, Co, and S elements (Figure 3b), and the existence of oxygen is possible due to the surface oxidation that occurs from the adsorption of water when the sample is exposed to an air atmosphere. As the high-resolution Co spectra of CoS_2 show in Figure 3c, the one pair of fitted peaks at 781.7 and 785.1 eV are indexed to the Co^{3+} and Co^{2+} of the spin-orbital of Co $2P_{3/2}$; another pair of peaks at 798.0 and 800.6 eV correspond to the Co^{3+} and Co^{2+} of the spin-orbital of Co $2p_{1/2}$, and the additional peaks

at 788.4 and 803.5 eV are the related satellite peaks, respectively. In comparison to CoS_2, two pairs of peaks for CoS_2@MoS_2 at 785.7/801.2 eV and 782.2/798.6 eV correspond to the Co^{2+} and Co^{3+} of the spin-orbital of Co $2p_{3/2}$ and Co $2p_{1/2}$, with related satellite peaks at 788.9 and 804.5 eV. It can be seen that the peaks for CoS_2@MoS_2 positively shifted to the high-energy region, while the Co 2p satellite peaks of CoS_2/MoS_2 are stronger than those of the pristine CoS_2, implying that the high-spin Co^{3+} is dominant [44]. The Mo 3d spectra can be deconvoluted to five peaks, as shown in Figure 3d. A pair of peaks at 229.2 and 232.3 eV is indexed to the 1 T of Mo $3d_{5/2}$ and Mo $3d_{3/2}$, two peaks at 229.9 and 233.2 eV are ascribed to the 2H phase of Mo $3d_{5/2}$ and Mo $3d_{3/2}$, and the additional peak at 236.1 eV corresponds to the oxidized Mo species, respectively [45]. The base of MoS_2 with the 2H phase is a sulfur-modified surface, which has poor catalytic activity [46], and the metallic 1T phase of MoS_2 can expose more active sites and improve the electronic conductivity [47]. The peak area of the 1T phase is larger than that of the 2H phase, implying that the metallic 1T phase is dominant for the pristine MoS_2. In comparison, CoS_2@MoS_2 shows a negative shift of Mo 3d peaks to the low-energy region. The negative shift of Mo 3d and the positive shift of Co 2p can be attributed to the strong chemical interaction at the CoS_2/MoS_2 interface by forming a Mo-S-Co bond [48]. Figure 3e shows the S 2p spectra of all catalysts and CoS_2@MoS_2 shows two peaks at 161.7 and 162.8 eV, corresponding to the spin-orbital of S $2p_{3/2}$ and S $2p_{1/2}$. The peaks of CoS_2@MoS_2 are positively shifted in contrast to CoS_2, and the peak at high binding energy is decreased, implying the strong interaction at the CoS_2/MoS_2 interface. The deconvoluted O 1s spectra can be deconvoluted into three dominant peaks, as shown in Figure 3f, including the metal–oxide bond (lattice oxygen, O^{2-}), defective oxygen with low oxygen coordination (oxygen vacancies, O^-), and the hydroxyl species or adsorbed oxygen on the surface (OH^-/O_2) [49].

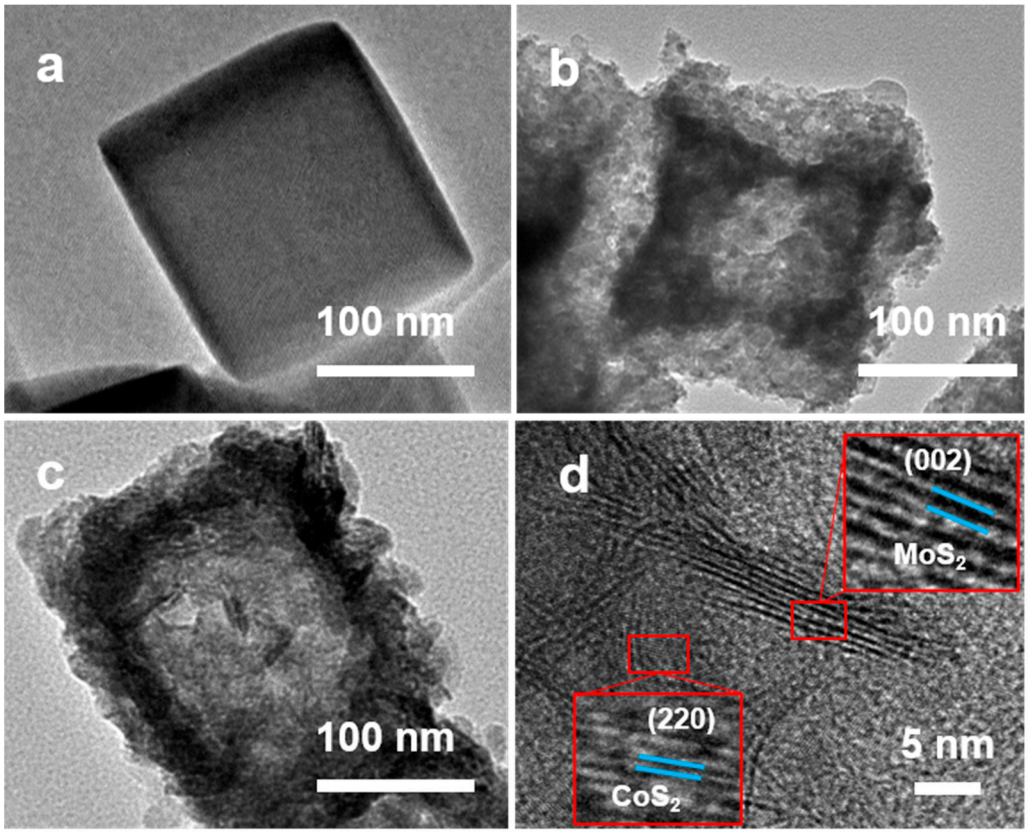

Figure 2. TEM images of (**a**) Co-PBA, (**b**) CoS_2, and (**c**) CoS_2@MoS_2. (**d**) HR-TEM image of CoS_2@MoS_2.

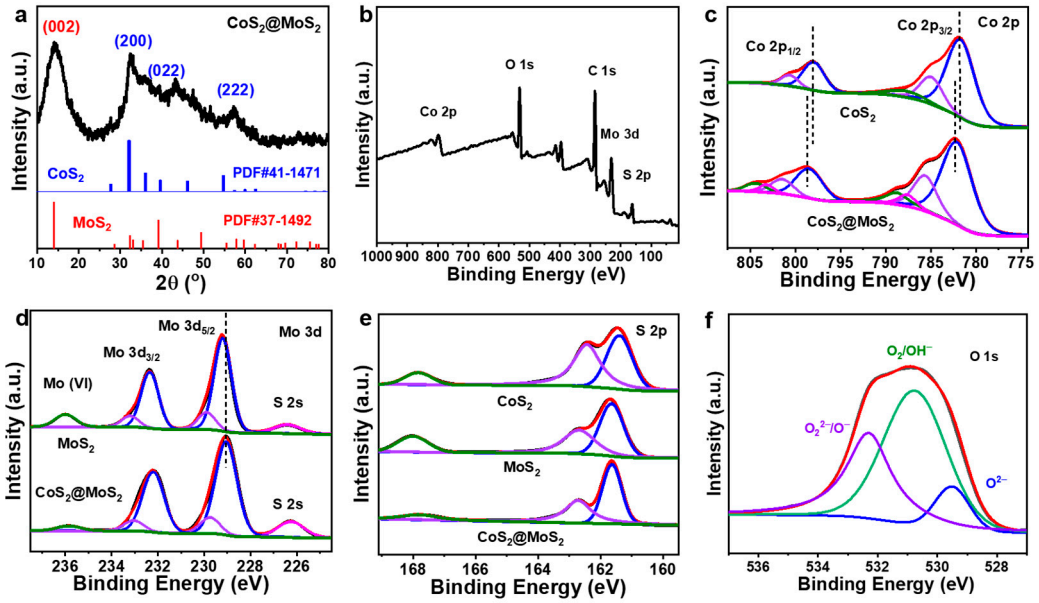

Figure 3. (**a**) XRD pattern of CoS_2@MoS_2. (**b**) Full XPS scan of CoS_2@MoS_2. High-resolution (**c**) Co 2p of CoS_2 and CoS_2@MoS_2, (**d**) Mo 3d of MoS_2 and CoS_2@MoS_2, (**e**) S 2p of CoS_2, MoS_2, and CoS_2@MoS_2, and (**f**) O 1s spectra of CoS_2@MoS_2.

2.2. Electrocatalytic Performance

The electrocatalytic OER performance of CoS_2@MoS_2 was evaluated via a three-electrode configuration in 1 M KOH electrolyte, and the electrolyte was treated by flowing nitrogen gas before measurement. Two additional catalysts of MoS_2 and CoS_2 as control samples were analyzed under the same conditions and all the overpotentials were calibrated after IR correction. Figure 4a shows the polarization curves of all catalysts at 5 mV s^{-1}. To reach the current density of 10 mA cm^{-2}, CoS_2 and MoS_2 show moderated overpotentials of 304 and 381 mV, and CoS_2@MoS_2 shows the highest OER performance with the smallest overpotential of 254 mV. At the high current density of 20 and t, CoS_2@MoS_2 exhibits overpotentials of 278 and 346 mV, which are both smaller than those of the control samples (Figure 4b). The Tafel slope, as an important factor in evaluating the kinetic HER behavior, was calculated by fitting the selected region of polarization curves in Figure 4c. The corresponding Tafel slope of CoS_2@MoS_2 is 86.9 mV dec^{-1}, which is much lower than that of pristine CoS_2 and MoS_2, implying its fast dynamic behavior and good catalytic performance. The value of the Tafel slope is between 40 and 120 mV dec^{-1}, revealing that the Volmer–Heyrovsky process is dominated as the rate-determined step [50]. Furthermore, electrochemical impedance spectroscopy (EIS) was carried out to further confirm the kinetic behavior of CoS_2@MoS_2 and unveil the high OER activity. Nyquist plots were deconvoluted by the equivalent circuit (inset of Figure 4d), in which Rs, R1, and Rct represent the solution resistance, the contact resistance on the surface of the electrode, and the charge transfer resistance. CoS_2@MoS_2 shows the smallest diameter of a semi-circle in the high-frequency region and the lowest Rct value (Figure 4d), indicating that CoS_2@MoS_2 has good electrical conductivity, permitting it to improve the electron transfer capability. The features of the Tafel slope and EIS analysis strongly prove that CoS_2@MoS_2 exhibits fast catalytic kinetics and exceptional catalytic OER performance owing to the core–shell structure and strong chemical coupling at the CoS_2@MoS_2 interface. In comparison, the catalytic OER activity of the core–shell CoS_2@MoS_2 catalyst with a low overpotential is also superior to the reported results shown in Figure 4e [22,51–58].

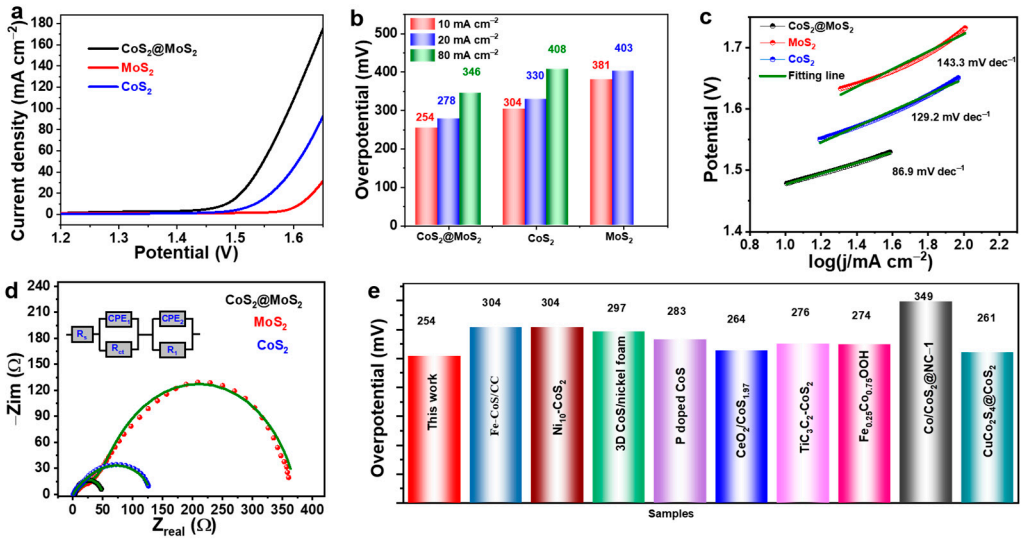

Figure 4. (**a**) Polarization curves of CoS_2, MoS_2, and CoS_2@MoS_2. (**b**) Overpotential of CoS_2, MoS_2, and CoS_2@MoS_2 at different current densities. (**c**) Tafel slopes and (**d**) Nyquist plots (inset: the equivalent circuit) of CoS_2, MoS_2, and CoS_2@MoS_2. (**e**) Comparison of overpotential with the reported results.

The kinetic behavior of the CoS_2@MoS_2 catalyst was further confirmed by active energy derived from the Arrhenius equation, and the related CV curves were measured at different temperatures of 25 °C, 35 °C, 45 °C, 55 °C, and 65 °C. As shown in Figure 5a, the overpotential of the CoS_2@MoS_2 catalyst gradually decreases along with the increased temperature, implying that the OER activity is significantly improved. Meanwhile, the CoS_2@MoS_2 catalyst at 65 °C shows the lowest Tafel slope value, indicating fast dynamic properties with the increase in temperature (Figure 5b). The active energy can be determined by fitting the 1/T vs. log (j) [59], and the value of log (j) is obtained from the intersection where the Tafel slope intersects with the x-axis. The value of active energy is 55.1 kJ mol^{-1} according to the linear fitting of the Arrhenius plot, as shown in Figure 5c.

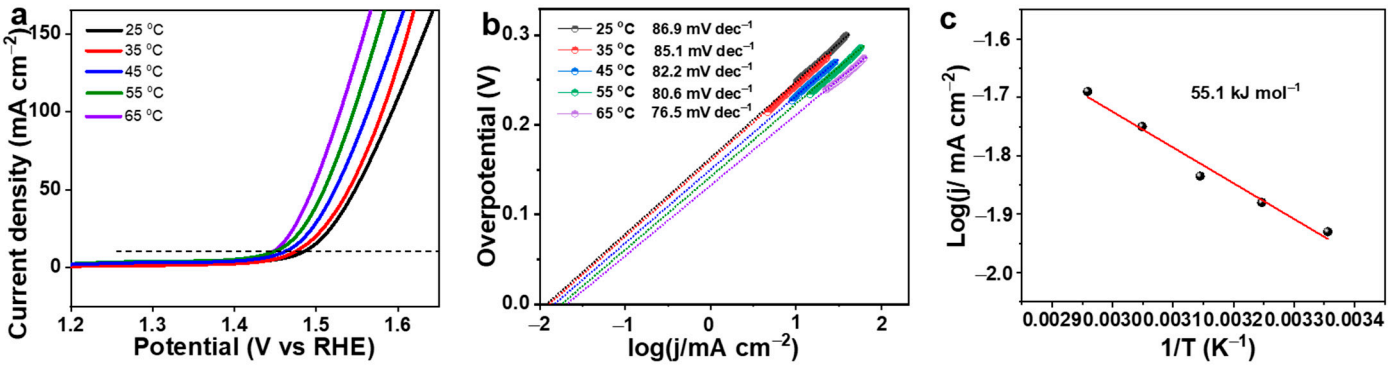

Figure 5. (**a**) Polarization curves and (**b**) Tafel slopes of CoS_2@MoS_2 catalyst at different temperatures. (**c**) Arrhenius plots of CoS_2@MoS_2 catalyst by linearly fitting 1/T vs. log (j).

To evaluate the catalytic behavior of the CoS_2@MoS_2 catalyst, the CV curves in the non-faradic reaction area were measured at a scan rate from 5 to 50 mV s^{-1} (Figure 6a–c), and the related double-layer capacitance (Cdl) was calculated by fitting the CV curves shown in Figure 6d. The value of Cdl for CoS_2@MoS_2 is 10.9 mF cm^{-2}, which is much higher than that of MoS_2 (0.65 mF cm^{-2}) and CoS_2 (5.8 mF cm^{-2}), predicting that the CoS_2@MoS_2 catalyst can expose abundant active sites on the surface to improve the electrocatalytic OER performance. The vertical growth of MoS_2 nanosheets on the surface of the CoS_2 nanocube not only prevents the restacking of layered MoS_2, but also exposes more marginal active

sites. The formed core–shell structure can provide many pathways for electrolyte diffusion and charge transfer and improve the utilization of active sites. The catalytic stability is an important consideration to evaluate the electrochemical performance of the catalyst during the OER process. The polarization curves of CoS_2@MoS_2 are initially measured by CV at 5 mV s^{-1} (Figure 6e), and almost no change of the curves at the 1st and 1001st cycles can be observed, revealing the high catalytic OER stability favored by the core–shell structure and CoS_2@MoS_2 formation. Meanwhile, a chronoamperometry (CA) test was further applied at the overpotential of 254 mV for 15 h (Figure 6f), and there was no apparent change in current density during the continuous operation, further demonstrating the exceptional catalytic stability.

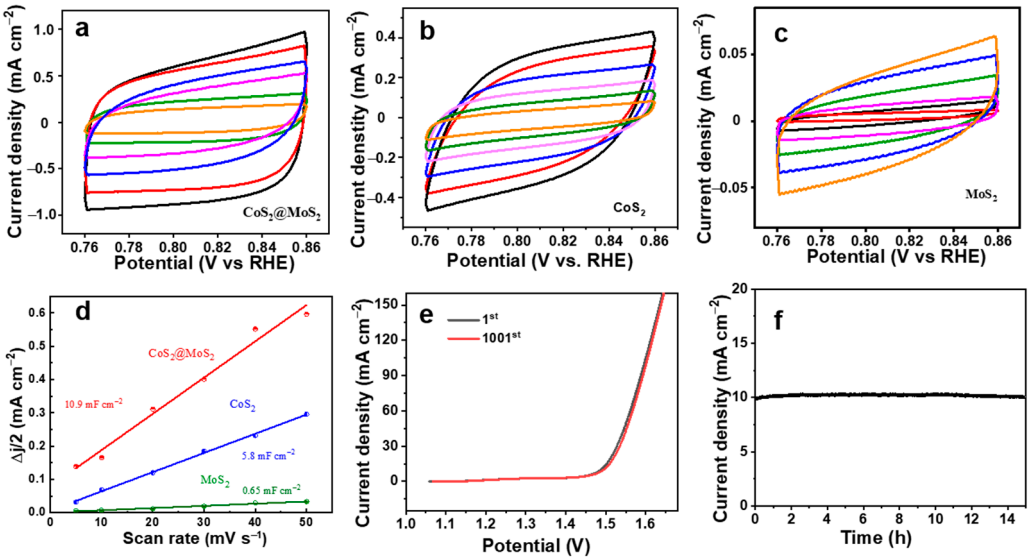

Figure 6. CV curves of (**a**) CoS_2@MoS_2, (**b**) CoS_2, and (**c**)MoS_2. (**d**) C_{dl} values of CoS_2, MoS_2, and CoS_2@MoS_2. (**e**) CV curves for CoS_2@MoS_2 at 1st and 1001st cycles and (**f**) CA test for 15 h.

The excellent electrocatalytic OER activity of CoS_2@MoS_2 in alkaline electrolytes can be ascribed to the synergistic effect of the core–shell structure and the generation of a heterostructure interface; the possible reasons for this are as follows. (1) The hollow CoS_2 with a nanocubic structure can act as the carrier to prevent the restacking of MoS_2 nanosheets and provide the pathways for fast electrolyte ion diffusion. (2) Layered MoS_2 nanosheets are vertically grown on the surface of CoS_2, the utilization of exposed marginal and basal active sites of CoS_2@MoS_2 can be improved, and the contact between the electrolyte and the electrode can be increased. (3) The core–shell structure, with CoS_2 as the core and MoS_2 as the shell, can provide abundant exposed active catalyst sites, improve the reaction rate, inhibit the aggregation of catalyst, accelerate water oxidation, and promote the adsorption/desorption of intermediates. (4) The different chemical components and crystal structure can induce the lattice strain to affect the absorbability of intermediates, and the charge transfer at the interface can adjust the electronic structure of the catalyst. (5) The strong chemical interaction at the CoS_2@MoS_2 interface can boost the active sites to improve the catalytic OER activity.

The change in the morphological structure and surface chemistry of CoS_2@MoS_2 after CA measurement in 1 M KOH was unveiled by SEM, TEM, and XPS. After the catalytic OER test, the roughness of the CoS_2@MoS_2 surface was observed and the transparency of the catalyst decreased, which was attributed to the formation of metal oxide/hydroxides and small residual components on the surface (Figure 7a,b). Figure 7c shows the high-resolution Co 2p spectra of CoS_2@MoS_2 before and after the CA test, and the major peaks of Co $2p_{3/2}$ and Co $2p_{1/2}$ shifted to the low-energy region arising from the surface oxidation of CoS_2@MoS_2 during the CA test using alkaline electrolytes, such as the intermediates

of cobalt oxides or oxyhydroxides. In particular, the peaks of CoS_2@MoS_2 become broad and negatively shift after the CA test in contrast to its pristine state, which is attributed to the change in the surface chemistry through the conversion of the metal-S bond to the metal-O bond during the stability test. Meanwhile, the Mo 3d spectra show two primary peaks of Mo $3d_{5/2}$ at 229.2 eV and Mo $3d_{3/2}$ at 232.1 eV, and an additional peak at 236.0 eV attributed to the formation of the Mo-O bond after the CA test (Figure 7d). The slight shift of the Mo 3d peaks and the presence of a strong Mo-O bond imply that the surface of the CoS_2@MoS_2 is oxidized.

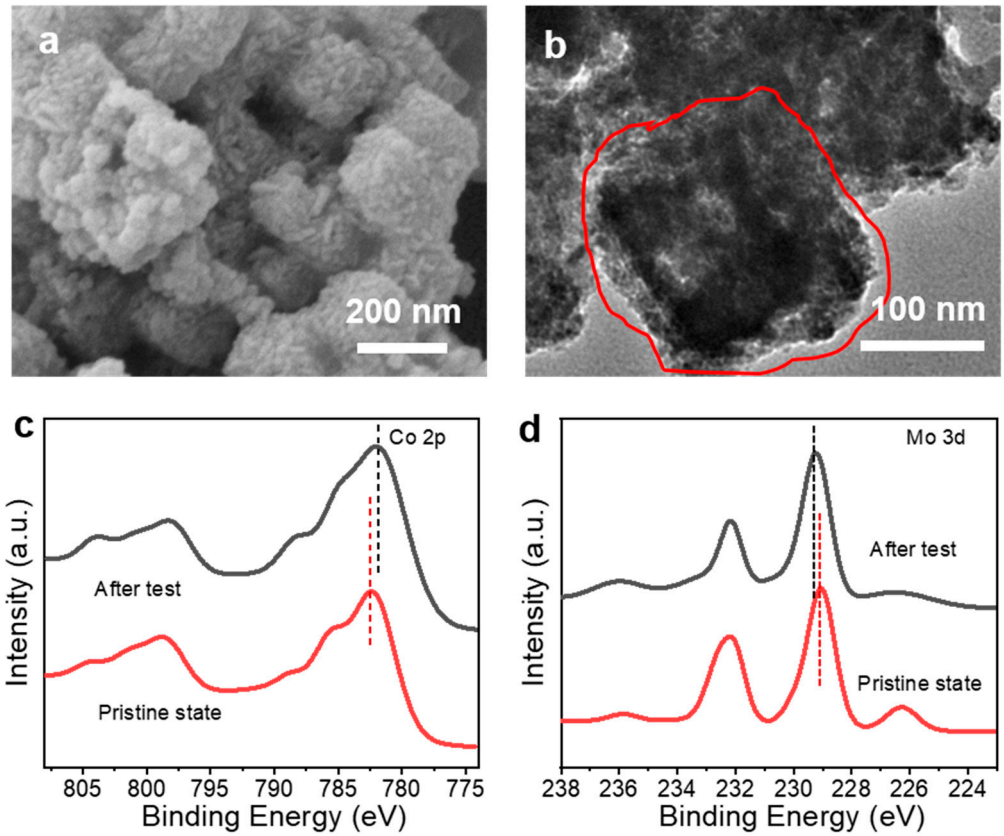

Figure 7. (**a**) SEM and (**b**) TEM images of CoS_2@MoS_2 after the CA test. High-resolution XPS spectra of CoS_2@MoS_2 before and after the CA test: (**c**) Co 2p and (**d**) Mo 3d.

3. Materials and Methods

3.1. Synthesis of Co-PBA

First, 150 mg of cobaltous chloride hexahydrate was mixed with 900 mg of sodium citrate dehydrate in 50 mL of deionized (DI) water under magnetic stirring for 30 min. Then, 50 mL of potassium hexacyanocobaltate (III) solution (about ~300 mg) was added into the above mixture drop by drop within 10 min under continuous stirring. After continuous aging at room temperature for 24 h, the solution was treated by centrifugation and the obtained precipitates were washed several times with DI water/ethanol. The precipitate was dried at 60 °C overnight and denoted as Co-PBA.

3.2. Synthesis of CoS_2

In total, 50 mg of the as-obtained Co-PBA was dispersed in 15 mL of ethanol under magnetic stirring for 1 h to obtain the dispersion. Then, 15 mL of sodium sulfide solution (4 mg mL^{-1}) in DI water was subsequently added into the dispersion under magnetic stirring for 10 min. The mixture was poured into a 50 mL Teflon-lined stainless-steel autoclave and heated at 120 °C for 10 h. After cooling down to room temperature, the

precipitate was centrifuged and washed several times with water/ethanol. Finally, the precipitate was thermally activated at 400 °C for 1 h under a N_2 atmosphere.

3.3. Synthesis of Pure MoS_2

In this step, 150 mg of thiourea and 80 mg of ammonium molybdate were dissolved in 30 mL of DI water under magnetic stirring for 1 h. The mixture was subsequently transferred into a 50 mL Teflon-lined stainless-steel autoclave and heated at 240 °C for 20 h and naturally cooled down to room temperature. The precipitate was centrifuged and washed several times with water/ethanol. Finally, the precipitate was thermally annealed at 400 °C for 1 h under a N_2 atmosphere.

3.4. Synthesis of Hollow CoS_2@MoS_2

Firstly, 50 mg of Co PBA was dispersed in 12 mL of ethanol under ultrasonication and 15 mL of sodium sulfide solution (4 mg mL^{-1}) in DI water was subsequently added into the dispersion under magnetic stirring for 10 min. Then, 150 mg of thiourea and 80 mg of ammonium molybdate were dissolved in 30 mL of DI water under magnetic stirring for 1 h, and the mixture was transferred into a 50 mL Teflon-lined stainless-steel autoclave and heated at 120 °C for 5 h and 240 °C for 20 h. The black precipitate was centrifuged and washed with DI water/ethanol following air-drying at 60 °C overnight. Finally, the product was obtained by thermal annealing at 400 °C for 1 h under a N_2 atmosphere and denoted as CoS_2@MoS_2.

3.5. Characterization

Powder X-ray diffraction (XRD) patterns were recorded on a Bruker D8 Advance powder X-ray diffractometer using a Cu Kα (λ = 1.5405 Å) radiation source operating at 40 kV and 40 mA with the scanning rate of 5° min^{-2}. The morphology and microstructure of the product were analyzed by scanning electron microscopy (FESEM, Hitachi, S-4800 II, Tokyo, Japan) and transmission electron microscopy (TEM, Philips, TECNAI 12, Amsterdam, Holland). All X-ray photoelectron spectroscopy (XPS) measurements were carried out on Kratos XSAM-800 spectrometers with an Al Kα radiation source.

3.6. Electrochemical Measurements

All of the electrochemical measurements were taken using a three-electrode configuration (CHI 660E electrochemical workstation). The catalyst ink deposited on a glassy carbon electrode (GCE) acted as the working electrode, while a graphite rod and saturated calomel electrode (SCE) worked as the counter and reference electrodes. The preparation of the catalytic ink is as follows: 5 mg of active material, 50 μL of Nafion, and 950 μL of ethanol were mixed under bath sonication for 20 min. Subsequently, 10 μL of the catalyst ink was deposited on the surface of the GCE and dried at room temperature (0.71 mg cm^{-2}). The potentials reported in the work were converted to the reversible hydrogen electrode (RHE) by $E_{(RHE)} = E_{(SCE)} + 0.0591 * pH + 0.242$ V.

The polarization curves were characterized by cyclic voltammetry (CV) at a scan rate of 5 mV s^{-1}, and electrochemical impedance spectroscopy (EIS) was conducted in the frequency range from 100 kHz to 0.01 kHz. Meanwhile, the CV curves in the non-faradic region were measured at scan rates from 5 to 50 mV s^{-1}. Chronoamperometry (CA) testing was carried out for 15 h.

4. Conclusions

Herein, we successfully prepared a core–shell-structured CoS_2@MoS_2 nanobox through precipitation, sulfurization, and hydrothermal methods. The vertical growth of MoS_2 nanosheets on the hollow CoS_2 matrix can effectively inhibit their aggregation and guarantee the exposure of active edge sites. The hollow morphology with a core–shell structure consisting of CoS_2 and MoS_2 can accelerate the ion diffusion and charge transfer, while the formed CoS_2/MoS_2 heterostructure can boost the number of catalytic active sites dur-

ing the OER process. Due to the morphological structure and adjusted chemical surface, CoS_2@MoS_2 exhibits exceptional catalytic OER performance. To reach the current density of 10 mA cm^{-2}, CoS_2@MoS_2 only requires the overpotential of 254 mV with a low Tafel slope, small charge transfer resistance, and good catalytic stability.

Author Contributions: Formal analysis, conceptualization, funding acquisition, writing—original draft, and investigation, D.G.; methodology, resources, and investigation, J.X.; investigation, G.L.; supervision, writing—review and editing, and resources, X.Y. All authors have read and agreed to the published version of the manuscript.

Funding: This research was funded by the Key Science and Technology Program of Henan Province (Grant number 222102240044), the Program for Science & Technology Innovation Talents in Universities of Henan Province [Grant number 24HASTIT006], and the Natural Science Foundation of Henan Province [Grant number 242300420045].

Institutional Review Board Statement: Not applicable.

Informed Consent Statement: Not applicable.

Data Availability Statement: Data are contained within the article.

Acknowledgments: We acknowledge the technical support at the Testing Center of Yangzhou University. The authors would like to thank the anonymous reviewers who helped to significantly improve the quality of the research article.

Conflicts of Interest: The authors declare no conflicts of interest.

References

1. Liu, C.; Bai, Y.; Li, W.; Yang, F.; Zhang, G.; Pang, H. In Situ Growth of Three-Dimensional MXene/Metal-Organic Framework Composites for High-Performance Supercapacitors. *Angew. Chem. Int. Ed. Engl.* **2022**, *61*, e202116282. [CrossRef] [PubMed]
2. Bai, Y.; Liu, C.; Chen, T.; Li, W.; Zheng, S.; Pi, Y.; Luo, Y.; Pang, H. MXene-Copper/Cobalt Hybrids via Lewis Acidic Molten Salts Etching for High Performance Symmetric Supercapacitors. *Angew. Chem. Int. Ed.* **2021**, *60*, 25318–25322. [CrossRef] [PubMed]
3. Zhao, X.; Li, W.-P.; Cao, Y.; Portniagin, A.; Tang, B.; Wang, S.; Liu, Q.; Yu, D.Y.W.; Zhong, X.; Zheng, X.; et al. Dual-Atom Co/Ni Electrocatalyst Anchored at the Surface-Modified $Ti_3C_2T_x$ MXene Enables Efficient Hydrogen and Oxygen Evolution Reactions. *ACS Nano* **2024**, *18*, 4256–4268. [CrossRef]
4. Hanan, A.; Nazim Lakhan, M.; Walvekar, R.; Khalid, M.; Prakash, C. Heteroatom-doped MXenes as Electrocatalysts for Hydrogen Evolution Reaction: A Review on the Recent Advances, Mechanisms and Prospects. *Chem. Eng. J.* **2024**, *483*, 149107. [CrossRef]
5. Ren, X.; Wu, T.; Sun, Y.; Li, Y.; Xian, G.; Liu, X.; Shen, C.; Gracia, J.; Gao, H.-J.; Yang, H.; et al. Spin-Polarized Oxygen Evolution Reaction Under Magnetic Field. *Nat. Commun.* **2021**, *12*, 2608. [CrossRef] [PubMed]
6. Kuang, Y.; Qiao, W.; Yang, F.; Feng, L. Electrochemical Hydrogen Evolution Efficiently Boosted by Interfacial Charge Redistribution in Ru/$MoSe_2$ Embedded Mesoporous Hollow Carbon Spheres. *J. Energy Chem.* **2023**, *85*, 447–454. [CrossRef]
7. Yu, X.; Lin, L.; Pei, C.; Ji, S.; Sun, Y.; Wang, Y.; Kim, J.K.; Park, H.S.; Pang, H. Immobilizing Bimetallic RuCo Nanoalloys on Few-layered MXene as a Robust Bifunctional Electrocatalyst for Overall Water Splitting. *Chem. Eur. J.* **2023**, *30*, e202303524. [CrossRef] [PubMed]
8. Pan, Y.; Gao, J.; Lv, E.; Li, T.; Xu, H.; Sun, L.; Nairan, A.; Zhang, Q. Integration of Alloy Segregation and Surface Co-O Hybridization in Carbon-Encapsulated CoNiPt Alloy Catalyst for Superior Alkaline Hydrogen Evolution. *Adv. Funct. Mater.* **2023**, *33*, 2303833. [CrossRef]
9. Li, T.-T.; Cui, J.-Y.; Xu, M.; Song, K.; Yin, Z.-H.; Meng, C.; Liu, H.; Wang, J.-J. Efficient Acidic Photoelectrochemical Water Splitting Enabled by Ru Single Atoms Anchored on Hematite Photoanodes. *Nano Lett.* **2024**, *24*, 958–965. [CrossRef]
10. Tu, W.; Chen, K.; Zhu, L.; Zai, H.E.B.; Ke, X.; Chen, C.; Sui, M.; Chen, Q.; Li, Y. Tungsten-Doping-Induced Surface Reconstruction of Porous Ternary Pt-Based Alloy Electrocatalyst for Oxygen Reduction. *Adv. Funct. Mater.* **2019**, *29*, 1807070. [CrossRef]
11. He, R.; Wang, C.; Feng, L. Amorphous FeCoNi-S as Efficient Bifunctional Electrocatalysts for Overall Water Splitting Reaction. *Chin. Chem. Lett.* **2023**, *34*, 107241. [CrossRef]
12. Lin, J.; Zhou, H.; Amin, R.S.; Fetohi, A.E.; El-Khatib, K.M.; Wang, C.; Guo, L.; Wang, Y. In situ Formation of Nickel Sulfide Quantum Dots Embedded into a Two-Dimensional Metal–Organic Framework for Water Splitting. *Inorg. Chem. Front.* **2023**, *10*, 1294–1304. [CrossRef]
13. Zhang, T.; Sun, J.; Guan, J. Self-Supported Transition Metal Chalcogenides for Oxygen Evolution. *Nano Res.* **2023**, *16*, 8684–8711. [CrossRef]
14. Chen, S.; Zhang, T.; Han, J.; Qi, H.; Jiao, S.; Hou, C.; Guan, J. Interface Engineering of Fe-Sn-Co Sulfide/Oxyhydroxide Heterostructural Electrocatalyst for Synergistic Water Splitting. *Nano Res. Energy* **2024**, *3*, e9120106. [CrossRef]

15. Huang, Y.; Jiang, L.-W.; Liu, H.; Wang, J.-J. Electronic Structure Regulation and Polysulfide Bonding of Co-doped $(Ni, Fe)_{1+x}S$ Enable Highly Efficient and Stable Electrocatalytic Overall Water Splitting. *Chem. Eng. J* **2022**, *441*, 136121. [CrossRef]
16. Hu, X.; Wang, R.; Feng, W.; Xu, C.; Wei, Z. Electrocatalytic Oxygen Evolution Activities of Metal Chalcogenides and Phosphides: Fundamentals, Origins, and Future Strategies. *J. Energy Chem.* **2023**, *81*, 167–191. [CrossRef]
17. Mijowska, E.; Pietrusewicz, K.; Maślana, K. Highly Porous Carbon Flakes Derived from Cellulose and Nickel Phosphide Heterostructure towards Efficient Electrocatalysis of Oxygen Evolution Reaction. *Molecules* **2024**, *29*, 352. [CrossRef]
18. Yuan, S.; Peng, J.; Cai, B.; Huang, Z.; Garcia-Esparza, A.T.; Sokaras, D.; Zhang, Y.; Giordano, L.; Akkiraju, K.; Zhu, Y.G.; et al. Tunable Metal Hydroxide–Organic Frameworks for Catalysing Oxygen Evolution. *Nat. Mater.* **2022**, *21*, 673–680. [CrossRef] [PubMed]
19. Fu, K.; Chen, W.; Jiang, F.; Chen, X.; Liu, J. Research Progress of Perovskite-Based Bifunctional Oxygen Electrocatalyst in Alkaline Conditions. *Molecules* **2023**, *28*, 7114. [CrossRef]
20. Yin, Z.-H.; Huang, Y.; Song, K.; Li, T.-T.; Cui, J.-Y.; Meng, C.; Zhang, H.; Wang, J.-J. Ir Single Atoms Boost Metal–Oxygen Covalency on Selenide-Derived NiOOH for Direct Intramolecular Oxygen Coupling. *J. Am. Chem. Soc.* **2024**, *146*, 6846–6855. [CrossRef]
21. Yu, J.; Qian, Y.; Seo, S.; Liu, Y.; Bui, H.T.D.; Tran, N.Q.; Lee, J.; Kumar, A.; Wang, H.; Luo, Y.; et al. Exploring Catalytic Behaviors of CoS_2-ReS_2 Heterojunction by Interfacial Engineering. *J. Energy Chem.* **2023**, *85*, 11–18. [CrossRef]
22. Kong, W.; Luan, X.; Du, H.; Xia, L.; Qu, F. Enhanced Electrocatalytic Activity of Water Oxidation in an Alkaline Medium via Fe Doping in CoS_2 Nanosheets. *Chem. Commun.* **2019**, *55*, 2469–2472. [CrossRef] [PubMed]
23. Yu, X.; Pan, Z.; Pei, C.; Lin, L.; Lu, Y.; Park, H.S.; Pang, H. Core-shell Heterostructure by Coupling Layered ReS_2 with Co_9S_8 Nanocubes for Boosted Oxygen Evolution Reaction. *Chin. Chem. Lett.* **2024**, *35*, 108484. [CrossRef]
24. Yang, G.; Pei, C.; Xu, F.; Park, H.S.; Yu, X.; Pang, H. Prussian Blue Analogue Derived $NiCoSe_4$ Coupling with Nitrogen-Doped Carbon Nanofibers for Pseudocapacitive Electrodes. *Chin. Chem. Lett.* **2023**, *34*, 108152. [CrossRef]
25. Lee, J.H.; Kattel, S.; Wang, Y.; Tackett, B.M.; Xie, Z.; Hwang, S.; Denny, S.R.; Xu, W.; Chen, J.G. Prussian Blue Analogues as Platform Materials for Understanding and Developing Oxygen Evolution Reaction Electrocatalysts. *J. Catal.* **2021**, *393*, 390–398. [CrossRef]
26. Chang, J.; Hu, Z.; Wu, D.; Xu, F.; Chen, C.; Jiang, K.; Gao, Z. Prussian Blue Analog-Derived Nickel Iron Phosphide-Reduced Graphene Oxide Hybrid as an Efficient Catalyst for Overall Water Electrolysis. *J. Colloid Interf. Sci.* **2023**, *638*, 801–812. [CrossRef]
27. Wang, L.; Wang, J.; Yan, L.; Ding, Y.; Wang, X.; Liu, X.; Li, L.; Ju, J.; Zhan, T. Prussian Blue Analogue-Derived Iron Sulfide–Cobalt Sulfide Nanoparticle-Decorated Hollow Nitrogen-Doped Carbon Nanocubes for the Selective Electrochemical Detection of Dopamine. *ACS Sustain. Chem. Eng.* **2022**, *10*, 17230–17240. [CrossRef]
28. Guo, Y.; Jia, K.; Dai, F.; Liu, Y.; Zhang, C.; Su, J.; Wang, K. Hierarchical Porous Tri-Metallic NiCoFe-Se/CFP Derived from Ni-Co-Fe Prussian Blue Analogues as Efficient Electrocatalyst for Oxygen Evolution Reaction. *J. Colloid Interf. Sci.* **2023**, *642*, 638–647. [CrossRef]
29. Pei, C.; Chen, H.; Dong, B.; Yu, X.; Feng, L. Electrochemical Oxygen Evolution Reaction Efficiently Catalyzed by a Novel Porous Iron-Cobalt-Fluoride Nanocube Easily Derived from 3-Dimensional Prussian Blue Analogue. *J. Power Sources* **2019**, *424*, 131–137. [CrossRef]
30. Sun, P.; Zhou, Y.; Li, H.; Zhang, H.; Feng, L.; Cao, Q.; Liu, S.; Wågberg, T.; Hu, G. Round-the-clock Bifunctional Honeycomb-like Nitrogen-Doped Carbon-Decorated Co_2P/Mo_2C-Heterojunction Electrocatalyst for Direct Water Splitting with 18.1% STH Efficiency. *Appl. Catal. B Environ.* **2022**, *310*, 121354. [CrossRef]
31. Ma, Y.; Leng, D.; Zhang, X.; Fu, J.; Pi, C.; Zheng, Y.; Gao, B.; Li, X.; Li, N.; Chu, P.K.; et al. Enhanced Activities in Alkaline Hydrogen and Oxygen Evolution Reactions on MoS_2 Electrocatalysts by In-Plane Sulfur Defects Coupled with Transition Metal Doping. *Small* **2022**, *18*, 2203173. [CrossRef]
32. Wu, K.; Li, X.; Wang, W.; Huang, Y.; Jiang, Q.; Li, W.; Chen, Y.; Yang, Y.; Li, C. Creating Edge Sites within the Basal Plane of a MoS2 Catalyst for Substantially Enhanced Hydrodeoxygenation Activity. *ACS Catal.* **2021**, *12*, 8–17. [CrossRef]
33. Ran, N.; Song, E.; Wang, Y.; Zhou, Y.; Liu, J. Dynamic Coordination Transformation of Active Sites in Single-Atom MoS_2 Catalysts for Boosted Oxygen Evolution Catalysis. *Energy Environ. Sci.* **2022**, *15*, 2071–2083. [CrossRef]
34. Chen, B.; Hu, P.; Yang, F.; Hua, X.; Yang, F.F.; Zhu, F.; Sun, R.; Hao, K.; Wang, K.; Yin, Z. In Situ Porousized MoS_2 Nano Islands Enhance HER/OER Bifunctional Electrocatalysis. *Small* **2023**, *19*, 2207177. [CrossRef]
35. Rong, M.; Mo, Y.; Zhou, S.; Ma, X.; Wang, S.; Cao, Z.; Zhong, H. Ce and MoS_2 Dual-Doped Cobalt Aluminum Layered Double Hydroxides for Enhanced Oxygen Evolution Reaction. *Int. J. Hydrogen Energy* **2022**, *47*, 1644–1655. [CrossRef]
36. Mu, X.; Zhu, Y.; Gu, X.; Dai, S.; Mao, Q.; Bao, L.; Li, W.; Liu, S.; Bao, J.; Mu, S. Awakening the Oxygen Evolution Activity of MoS_2 by Oxophilic-Metal Induced Surface Reorganization Engineering. *J. Energy Chem.* **2021**, *62*, 546–551. [CrossRef]
37. Chakraborty, S.; Marappa, S.; Agarwal, S.; Bagchi, D.; Rao, A.; Vinod, C.P.; Peter, S.C.; Singh, A.; Eswaramoorthy, M. Improvement in Oxygen Evolution Performance of NiFe Layered Double Hydroxide Grown in the Presence of 1T-Rich MoS_2. *ACS Appl. Mater. Interfaces* **2022**, *14*, 31951–31961. [CrossRef] [PubMed]
38. Lu, G.; Huang, X.; Li, Y.; Zhao, G.; Pang, G.; Wang, G. Covalently Integrated Core-Shell MOF@COF Hybrids as Efficient Visible-Light-Driven Photocatalysts for Selective Oxidation of Alcohols. *J. Energy Chem.* **2020**, *43*, 8–15. [CrossRef]
39. Huang, X.; Yu, L.; Wang, X.; Feng, L. Insights into Fe-Doping Effect-Induced Heterostructure Formation for the Oxygen Evolution Reaction. *Chem. Commun.* **2023**, *59*, 12294–12297. [CrossRef]

40. Hu, J.; Li, Z.; Zhao, D.; Han, Z.; Wu, X.; Zhai, J.; Liu, Z.; Tang, Y.; Fu, G. l-Lysine-Induced Green Synthesis of CoS/Co_3O_4 Nanoframes for Efficient Electrocatalytic Oxygen Evolution. *Green Chem.* **2023**, *25*, 7309–7317. [CrossRef]
41. Jiang, J.; Sun, R.; Huang, X.; Xu, W.; Zhou, S.; Wei, Y.; Han, S.; Li, Y. In-situ Derived Mo-doped NiCoP and MXene to Form Mott-Schottky Heterojunction with Tunable Surface Electron Density to Promote Overall Water Splitting. *Compos. Part B Eng.* **2023**, *263*, 110834. [CrossRef]
42. Yin, C.; Yang, F.; Wang, S.; Feng, L. Heterostructured $NiSe_2/MoSe_2$ Electronic Modulation for Efficient Electrocatalysis in Urea Assisted Water Splitting Reaction. *Chin. J. Catal.* **2023**, *51*, 225–236. [CrossRef]
43. Guo, Y.; Tang, J.; Henzie, J.; Jiang, B.; Xia, W.; Chen, T.; Bando, Y.; Kang, Y.-M.; Hossain, M.S.A.; Sugahara, Y.; et al. Mesoporous Iron-doped $MoS_2/CoMo_2S_4$ Heterostructures through Organic–Metal Cooperative Interactions on Spherical Micelles for Electrochemical Water Splitting. *ACS Nano* **2020**, *14*, 4141–4152. [CrossRef] [PubMed]
44. Frost, D.C.; McDowell, C.A.; Woolsey, I.S. Evidence for Multiplet Splitting of 2p Photoelectron Lines of Transition Metal Complexes. *Chem. Phys. Lett.* **1972**, *17*, 320–323. [CrossRef]
45. Mahmood, Q.; Park, S.K.; Kwon, K.D.; Chang, S.-J.; Hong, J.-Y.; Shen, G.; Jung, Y.M.; Park, T.J.; Khang, S.W.; Kim, W.S.; et al. Transition from Diffusion-Controlled Intercalation into Extrinsically Pseudocapacitive Charge Storage of MoS_2 by Nanoscale Heterostructuring. *Adv. Energy Mater.* **2015**, *6*, 1501115. [CrossRef]
46. Yang, F.; Hu, P.; Yang, F.F.; Chen, B.; Yin, F.; Hao, K.; Sun, R.; Gao, L.; Sun, Z.; Wang, K.; et al. CNTs Bridged Basal-Plane-Active 2H-MoS_2 Nanosheets for Efficient Robust Electrocatalysis. *Small* **2023**, *19*, 2301468. [CrossRef]
47. Wang, G.; Zhang, G.; Ke, X.; Chen, X.; Chen, X.; Wang, Y.; Huang, G.; Dong, J.; Chu, S.; Sui, M. Direct Synthesis of Stable 1T-MoS2 Doped with Ni Single Atoms for Water Splitting in Alkaline Media. *Small* **2022**, *18*, 2107238. [CrossRef] [PubMed]
48. Pei, C.; Kim, M.-C.; Li, Y.; Xia, C.; Kim, J.; So, W.; Yu, X.; Park, H.S.; Kim, J.K. Electron Transfer-Induced Metal Spin-Crossover at $NiCo_2S_4/ReS_2$ 2D–2D Interfaces for Promoting pH-universal Hydrogen Evolution Reaction. *Adv. Funct. Mater.* **2023**, *33*, 2210072. [CrossRef]
49. Zhang, H.; Guan, D.; Gu, Y.; Xu, H.; Wang, C.; Shao, Z.; Guo, Y. Tuning Synergy Between Nickel and Iron in Ruddlesden–Popper Perovskites through Controllable Crystal Dimensionalities towards Enhanced Oxygen-Evolving Activity and Stability. *Carbon Energy* **2024**, e465. [CrossRef]
50. Anantharaj, S.; Noda, S.; Driess, M.; Menezes, P.W. The Pitfalls of Using Potentiodynamic Polarization Curves for Tafel Analysis in Electrocatalytic Water Splitting. *ACS Energy Lett.* **2021**, *6*, 1607–1611. [CrossRef]
51. Guo, P.; Wu, Y.-X.; Lau, W.-M.; Liu, H.; Liu, L.-M. CoS Nanosheet Arrays Grown on Nickel Foam as an Excellent OER Catalyst. *J. Alloys Compd.* **2017**, *723*, 772–778. [CrossRef]
52. Mathankumar, M.; Karthick, K.; Nanda kumar, A.K.; Kundu, S.; Balasubramanian, S. In Situ Decorated Ni Metallic Layer with CoS2-Layered Thin Films via a Layer-by-Layer Strategy Using Pulsed Laser Deposition for Enhanced Electrocatalytic OER. *Inorg. Chem.* **2021**, *60*, 8946–8957. [CrossRef] [PubMed]
53. Li, Z.; Li, C.; Huang, J.; Sun, W.; Cheng, W.; He, C.; Tian, L. Structure Engineering of Amorphous P–CoS Hollow Electrocatalysts for Promoted Oxygen Evolution Reaction. *Int. J. Hydrogen Energy* **2022**, *47*, 15189–15197. [CrossRef]
54. Dai, T.; Zhang, X.; Sun, M.; Huang, B.; Zhang, N.; Da, P.; Yang, R.; He, Z.; Wang, W.; Xi, P.; et al. Uncovering the Promotion of $CeO_2/CoS_{1.97}$ Heterostructure with Specific Spatial Architectures on Oxygen Evolution Reaction. *Adv. Mater.* **2021**, *33*, 2102593. [CrossRef] [PubMed]
55. Devi, S.B.; Navamathavan, R. One-Pot Hydrothermal Synthesis of Ti_3C_2 (MXene)-CoS_2 Nanocomposite as a Bifunctional Electrocatalyst (HER/OER) for a Clean Environment. *J. Electrochem. Soc.* **2023**, *170*, 096503. [CrossRef]
56. Qian, L.-H.; Dong, W.-W.; Cao, Y.-B.; Ma, R.; Ding, Y.; Wang, X. ZIF-67-Derived $CuCo_2S_4$@CoS_2 as an Efficient Bifunctional Electrocatalyst for Overall Water Splitting. *New J. Chem.* **2023**, *47*, 20574–20582. [CrossRef]
57. Li, W.; Feng, X.; Zeng, X.; Gong, C.; Chen, X.; Li, D.; Zeng, Y.; Wang, X.; Pan, X.; Shi, Z.; et al. ZIF-8@ZIF-67 Derived Fe–CoS_2/CNT Carbon Polyhedron for Enhanced Electrocatalytic Oxygen Evolution Reaction. *Int. J. Hydrogen Energy* **2024**, *51*, 20–29. [CrossRef]
58. Gao, G.; Fang, B.; Ding, Z.; Dong, W.; Li, Y.-X.; Wang, X.L.; Yao, Y.-F. Co/CoS_2 Heterojunction Embedded in Nitrogen-Doped Carbon Framework as bifunctional Electrocatalysts for Hydrogen and Oxygen Evolution. *Int. J. Hydrogen Energy* **2023**, *48*, 1831–1841. [CrossRef]
59. Niu, H.-J.; Yan, Y.; Jiang, S.; Liu, T.; Sun, T.; Zhou, W.; Guo, L.; Li, J. Interfaces Decrease the Alkaline Hydrogen-Evolution Kinetics Energy Barrier on NiCoP/$Ti_3C_2T_x$ MXene. *ACS Nano* **2022**, *16*, 11049–11058. [CrossRef]